X-RAY REFLECTIVITY AND DIFFRACTION STUDIES OF LIQUID SURFACES AND SURFACTANT MONOLAYERS

Jens Als-Nielsen and Kristian Kjær

Physics Department
Risø National Laboratory
DK-4000 Roskilde, Denmark

1. INTRODUCTION

The structure of matter on a molecular length scale can be revealed by diffraction studies using radiation with wavelength in the Ångstrøm region. If the radiation couples weakly to the scattering objects, as is the case for neutrons and X-rays (but not for electrons), the interpretation of the diffraction pattern in terms of the underlying structure becomes particularly simple and reliable due to the validity of the Born approximation, which in this context is also called kinematical diffraction. On the other hand, if the coupling is weak, the beam has to be sufficiently intense and/or the sample must be of sufficient size to obtain an accurate diffraction pattern within a reasonable time. In a surface structure the number of diffracting atoms, confined within a nanometer thick surface layer, is comparatively small.

For this reason neutron diffraction has not yet been developed to be a significant tool in surface science although neutrons are sensitive to magnetism and to hydrogen locations by the use of a controlled isotopic ratio of protons to deuterons.

Very intense X-ray beams are now available in synchrotron radiation laboratories, and surface X-ray diffraction methods have been developed concomitantly. In this paper we shall confine ourselves to describing methods for studying surfaces of **liquids**. These can be simple liquids such as water or methanol for which the surface diffuseness due to thermal fluctuations has been determined[1], they can be liquid crystals with smectic layering near the free surface[2], or they can be heterogeneous systems such as a monolayer of amphiphilic molecules on a water surface[3].

It is useful to distinguish between two geometries of the diffraction experiment as shown in Fig. 1.1. **Specular reflection**, shown in the top part has a wavevector transfer $\mathbf{Q}$ perpendicular to the liquid surface and thus measures the average density variation across the surface. In the **diffraction** geometry, shown in the bottom part, surface sensitivity is obtained by means of grazing incidence of the incoming beam. In-plane structure of the surface is probed by scanning the angle 2θ or the corresponding horizontal wavevector transfer Q_{hor}. For fixed 2θ or Q_{hor} the intensity variation with Q_z as observed, e.g., with a vertical position sensitive detector reflects the structure perpendicular to the surface just as does specular reflection. Nevertheless the two methods do not necessarily provide identical information. If, for example, we consider a monolayer film on water with coexisting two-dimensional

T. Riste et al. (eds.), *Phase Transitions in Soft Condensed Matter*

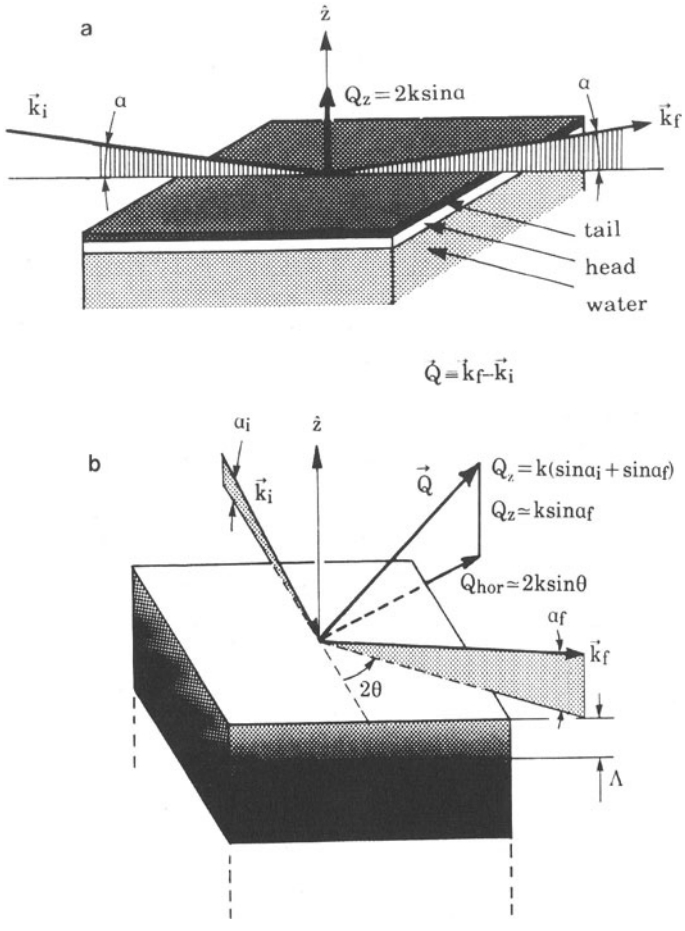

Fig. 1.1. Top: Specular reflection geometry probes the density profile across the interface.
Bottom: By grazing incidence the X-ray penetration depth Λ can be limited to a few nanometers. The evanescent wave is diffracted by the in-plane structure of the Langmuir film.

crystalline and liquid phases, the Q_z variation of intensity at 2θ corresponding to Bragg reflection from the crystalline phase reflects the thickness of the crystallites only, whereas the specular reflection pattern measures some sort of average thickness of the liquid and crystalline film.

The paper is organized as follows. First we recall and discuss Snell's and Fresnel's laws for X-ray optics. We then derive the general relation of the density profile across the surface to specular reflectivity (Fig. 1.1a) and to the Q_z–variation in grazing incidence diffraction (Fig. 1.1b). Specular reflectivity is illustrated by two examples. The first is reflection from a bare water surface and the determination of the diffuseness of the air-water interface due to thermally excited capillary waves. In the second example we consider a monomolecular film of an amphiphilic molecule, arachidic acid, floating on water, as the area per molecule is varied by a moveable barrier in a Langmuir trough[4].

The reflectivity data, analyzed in terms of a smeared box model of the molecular density, suggests that the hydrocarbon tails are close-packed but tilt uniformly as more area becomes available per molecule.

The grazing incidence diffraction (GID) technique is used to examine the molecular structure of the arachidic acid film in more detail. By mapping the intensity variation with both 2θ and α_f (Fig. 1.1b) we find:

(i) In the most compressed phase the molecules are upright and form a hexagonal lattice.
(ii) As the pressure is released the molecules tilt towards their nearest neighbours and the hexagonal lattice becomes uniaxially distorted in the direction of tilt.
(iii) The tilt angle and the density profile deduced from the GID data are consistent with the interpretation of the specular reflection data.

2. X-RAY OPTICS

For X-rays or neutrons of wave vector k the refractive index, n, of a medium can be simply related to the scattering properties of the medium, see, e.g., appendix of Ref. 3. For X-rays the relevant parameters are the Thompson scattering length of a single electron, r_0, and the electron density, ρ_{el}:

$$n = 1 - \delta, \qquad \delta = 2\pi\rho_{el} r_0 k^{-2}$$

Here, for simplicity we have neglected absorption effects and effects occurring when the photon energy is close to a resonance between the electron shells of the atom. The geometry of refraction at a sharp interface is as depicted in Fig. 2.1 with the angles α and α' being related by Snell's law: $\cos(\alpha)/\cos(\alpha') = n$. Since n is only very slightly less than unity (and can be written as $n = 1-\alpha_c^2/2$)

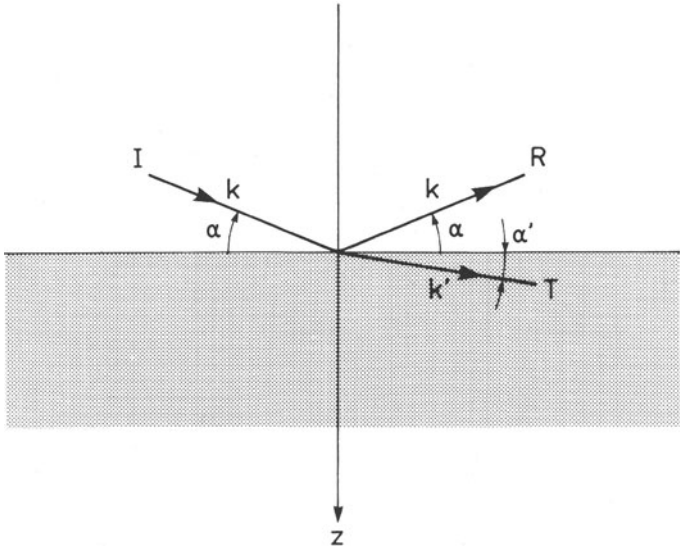

Fig. 2.1. The geometry of glancing incidence reflection and transmission at a discontinuous interface.

all glancing angles are small and expansion of Snell's law yields

$$\alpha^2 = \alpha'^2 + \alpha_c^2$$

The reflectivity R_F is the square of the ratio of the reflected and incident wave amplitudes. For small angles the Fresnel law for a sharp interface becomes particularly simple. The corresponding Fresnel reflectivity R_F is

$$R_F = |(\alpha - \alpha')/(\alpha + \alpha')|^2 \underset{\alpha \gg \alpha_c}{\rightarrow} (\alpha_c/2\alpha)^4 . \qquad (2.1)$$

Similarly one finds the transmitted or refracted wave intensity T_F, normalised to the incident intensity,

$$T_F = |2\alpha/(\alpha + \alpha')|^2 . \qquad (2.2)$$

Snell's and Fresnel's laws are derived by satisfying the boundary conditions for the X-ray wave fields at the interface.

Next, to include absorption effects in the refractive index, n, consider a plane wave, exp(−ikz), at normal incidence on a semi-infinite medium with linear absorption coefficient μ. On entering the medium the wavevector is changed to nk. We would like to write the plane wave in the medium as exp(−inkz), but we require an exponentially decaying **amplitude** exp(-μz/2). Formally, this is obtained by letting n be a complex number with an imaginary part −iβ, with the relation to μ given by equating − βkz with −μz/2 or β = μ/(2k). Including absorption effects thus leads to a complex index of refraction

$$n = 1 - \delta - i\beta \qquad (2.3)$$

with

$$\alpha_c^2 = 2\delta = 4\pi r_0 k^{-2} \rho_{e\ell} (1 + f'/Z) \qquad (2.4)$$

and

$$\beta = \mu/(2k) = 2\pi r_0 k^{-2} \rho_{e\ell} (f''/Z) \qquad (2.5)$$

In Eqs. (2.4) and (2.5), f ' and f " are the real and imaginary parts of the anomalous dispersion correction to the atomic scattering factor[5], which can be important when the X-ray energy is close to an absorption edge. Z is the number of electrons. Below, for simplicity, such effects will be assumed to be included in the electron densities, when necessary.

Including absorption effects, Snell's law for small angles becomes

$$\alpha^2 = \alpha'^2 + \alpha_c^2 + i2\beta \qquad (2.6)$$

whereas the expressions (2.1) and (2.2) remain valid using α' from Eq. 2.6.

The z-dependence of the transmitted wave amplitude is exp(−ik'α'z) which is proportional to exp(−k'Im(α')z). The 1/e depth for the intensity, Λ, is thus given by $\Lambda^{-1} = 2k'\mathrm{Im}(\alpha')$. However, for X-rays the deviation of n from unity is very small and the difference in **length** between k and k' can be neglected. The results for R_F, T_F and Λ depend on several parameters: The incident angle α, density and absorption in the medium, as well as the wavevector. In order to

get an overview of this multi-parameter problem it is convenient to use suitable units and to estimate orders of magnitudes. The natural unit for angles is the critical angle α_c. However, in connection with diffraction and reflection phenomena from non-homogeneous media, the wavevector transfer $Q_z \equiv 2k\sin(\alpha) \approx 2k\alpha$ is a more useful variable than just the grazing angle α. The natural unit for Q_z is $Q_c = 2k\alpha_c$ which, incidentally, varies only slightly with substance: $Q_c = 0.0217$ Å^{-1} for a light material such as water and $Q_z = 0.0678$ Å^{-1} for a heavy material like mercury. In terms of the dimensionless quantities x and x' for wavevector transfer and b for absorption

$$x \equiv Q_z/Q_c = \alpha/\alpha_c, \quad x' \equiv 2k\alpha'/Q_c = Q_z'/Q_c = \alpha'/\alpha_c \quad (\text{complex}), \quad b \equiv -(2\mu k/Q_c^2), \tag{2.7}$$

with x' determined from the dimensionless form of Eq. 2.6

$$x^2 = x'^2 + 1 + i(2b) \tag{2.8}$$

and recalling explicitly the formula for Q_c (cf. Eq. 2.4):

$$Q_c = 4(\pi\rho_{e\ell} r_0)^{1/2} \tag{2.9}$$

the final formulas for R_F, T_F and Λ become

$$R_F(x) = |(x - x')/(x + x')|^2, \tag{2.10}$$

$$T_F(x) = |2x/(x + x')|^2, \tag{2.11}$$

$$\Lambda^{-1}(x) = Q_c \, \mathrm{Im}(x'). \tag{2.12}$$

Fig. 2.2 (left part) shows from top to bottom graphs of R_F, ΛQ_c, T_F and the phase of the reflected wave for different absorption parameters b. For $x \geq 1.4$, the dependence on absorption is very small and the four quantities are compared to their asymptotic forms in the right part of Fig. 2.2. It may be useful to discuss separately the two limiting cases $\alpha \gg \alpha_c$ and $\alpha \ll \alpha_c$ as well as the special case of $\alpha = \alpha_c$.

(i) $x >> 1$ or $\alpha >> \alpha_c$:

In this case the solution for x' in Eq. 2.8 yields $\mathrm{Re}(x') \approx x$ and $\mathrm{Im}(x') \approx -b/x$. From Eq. 2.10 we find $R_F(x) \approx 1/(2x)^4$, in phase with the incident wave . The incident wave is almost completely transmitted though the interface, and the penetration depth is α/μ. The reflected intensity falls off as

$$R_F \rightarrow (Q_c/2Q_z)^4 \tag{2.13}$$

(ii) $x << 1$ or $\alpha << \alpha_c$:

In this case x' is almost purely imaginary with $\mathrm{Im}(x') \approx 1$, implying a reflectivity $R_F(x)$ close to unity. The reflected wave is out of phase with the incident wave, so the transmitted wave becomes very weak. It propagates nealy **parallel** to the surface with a minimal penetration depth of Q_c^{-1}, independent of α for $\alpha << \alpha_c$. Due to its small penetration depth, the wave field below the interface is called an **evanescent** wave.

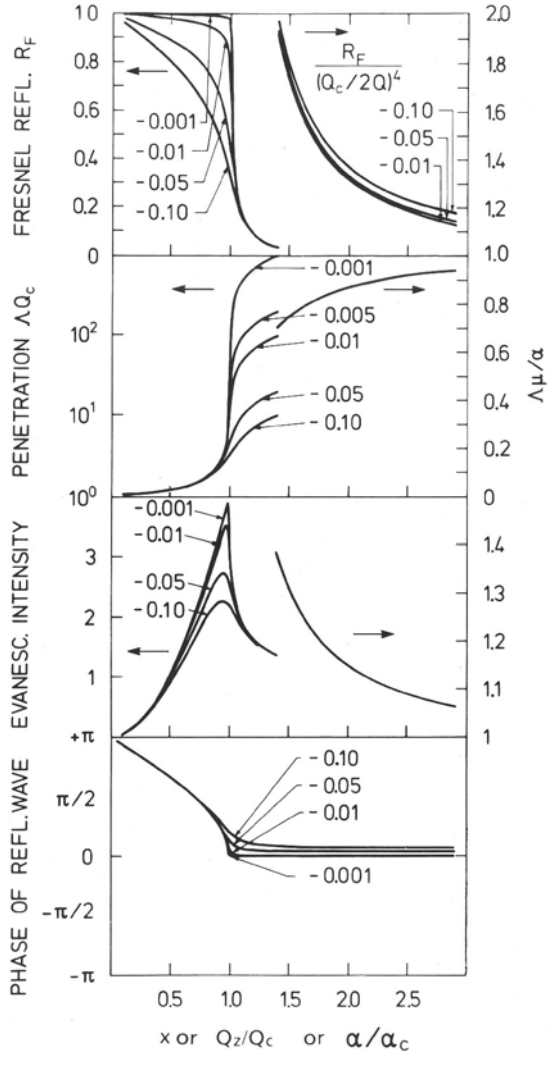

Fig. 2.2. Dependence on $x=Q_z/Q_c=a/a_c$ of reflectivity, penetration depth, evanescent wave intensity and phase difference between reflected and incident wave for various values of the absorption parameter b.

(iii) $x = 1$ or $\alpha = \alpha_c$:

From Eq. 2.8 we find $x' = |b|^{1/2}(1 + i)$. Since $b \ll 1$, $R_F(x) \approx 1$. The reflected wave is in phase with the incident wave implying that the evanescent wave **amplitude** approaches twice the incident wave amplitude. The penetration depth from Eq. 2.12 becomes $|b|^{-1/2}$ times larger than that for $x \ll 1$.

In summary then, we have considered reflected and transmitted waves for a grazing X-ray beam incident on a homogeneous, planar substance with a sharp interface. The transmitted wave intensity has a finite 1/e penetration depth Λ, partly due to ordinary absorption in the medium, but mainly due to the phenomenon of total external reflection. When the grazing angle α is less than the critical angle α_c the transmitted wave propagates exactly parallel to the surface when ordinary absorption is neglected, and almost parallel to the surface for the absorption occurring in practice. This wave is called the **evanescent** wave. For $\alpha > \alpha_c$ the reflected wave has a finite intensity approaching $(\alpha_c/2\alpha)^4$ for $\alpha \gg \alpha_c$.

For quantitative results at given wavevector k and a given material one first calculates the critical wavevector Q_c using Eq. 2.9 and the absorption parameter b using Eq. 2.7. With this information figure 2.2 can be used directly to estimate penetration depth, reflectivity or evanescent intensity. For more accurate work use formulas 2.8 and 2.10-12 recalling that the quantity x' is a complex number.

3. SPECULAR REFLECTIVITY AND INTERFACIAL DENSITY PROFILE

On an atomic length scale the interface between the liquid and the vapour above it is not sharp. In this section we shall see how the specular reflectivity $R(Q_z)$ at wavevector transfer Q_z is changed accordingly from the Fresnel reflectivity $R_F(Q_z)$. The electron density profile is denoted $\rho(z)$ and the density gradient $\rho'(z)$, see Fig. 3.1.

In order to derive $R(Q_z)$ we consider the reflected wave as a superposition of waves reflected from infinitesimal planes at varying depth z, implying the phase factor $\exp[iQ_z \cdot z]$. At first we neglect refraction and absorption effects. The reflectivity of a thin plate[6] with thickness Δz can be derived from the following simple dimensional argument. The reflected wave is the result of Thompson scattering of the incident photon wave by the individual electrons. The reflected **amplitude** ΔA_r must be proportional to the incident amplitude A_i, to the scattering length of a single electron and to the number of electrons per unit area perpendicular to the incident beam, $\rho(z)\Delta z/\sin\alpha$. Since $\Delta A_r/A_i$ is dimensionless and the dependence on quantities with dimensions of length such as scattering length, density and plate thickness is exhausted by their product, the only additional length in the problem, the X-ray wavelength λ must enter linearly. Hence,

$$\begin{aligned} \frac{\Delta A_r}{A_i} &= c \cdot \lambda \cdot r_0 \cdot \rho(z)\Delta z/\sin\alpha \\ &= c(4/Q_z)|\pi\rho_\infty r_0| \cdot \rho(z)/\rho_\infty \cdot \Delta z \\ &= c(Q_c^2/4Q_z) \cdot \rho(z)/\rho_\infty \cdot \Delta z \end{aligned} \qquad (3.1)$$

$$k = 2\pi/\lambda$$

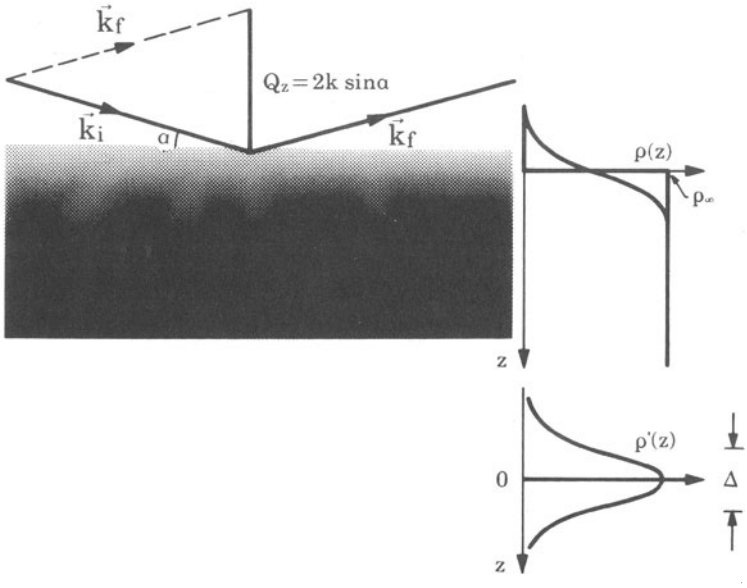

Fig. 3.1. The density variation across a surface is indicated by shading in the left part and more quantitatively by the function $\rho(z)$ in the right part. The reflectivity versus wavevector transfer Q_z is related to the Fourier transform of the gradient of the density, $\rho'(z)$.

using Eq. (2.9) for Q_c. Here, c is a dimensionless constant to be determined, and ρ_∞ is the electron density below the interface region.

The resulting reflected wave amplitude A_r is obtained by integration of Eq. (3.1) with the appropriate phase factor $\exp[iQ_z z]$ included. We find

$$\frac{A_r}{A_i} = (c/i)(Q_c/2Q_z)^2 \phi(Q_z) \tag{3.2}$$

with

$$\phi(Q_z) = iQ_z \rho_\infty^{-1} \int \rho(z) \exp[iQ_z z]\, dz \tag{3.3}$$

$$= \rho_\infty^{-1} \int \frac{d\rho(z)}{dz} \cdot \exp[iQ_z \cdot z] dz \tag{3.4}$$

being the Fourier transform of the gradient of the density profile across the interface. In the limit of a sharp interface the density gradient approaches a delta-function, $\phi(Q_z)$ approaches unity and the reflectivity is

$$(A_r/A_i)_F^2 = |c|^2 \cdot (Q_c/2Q_z)^4 \cdot 1 \tag{3.5}$$

In this derivation we have neglected refracting effects, which is equivalent to $Q_z \gg Q_c$. We saw in the previous section that in this limit $R_F = (Q_c/2Q_z)^4$ so we conclude that $|c|^2 = 1$ and are lead to the conjecture

$$R(Q_z) \simeq R_F(Q_z) \cdot |\phi(Q_z)|^2 , \tag{3.6}$$

replacing $(Q_c/2Q_z)^4$ by the general form $R_F(Q_z)$.

We discuss the limits of validity of the **master formula** (3.6): In the superposition of reflected waves from thin plates we used the phase factor $\exp[iQ_z z]$ with $Q_z = 2k\sin\alpha$. A more accurate phase than $Q_z z$ would be $Q'_z z = 2k\sin\alpha' \cdot z$ with $\alpha' = (\alpha^2 - \alpha_c^2)^{\frac{1}{2}}$.

Furthermore, multiple scattering effects have been neglected, e.g., a reflected wave from a thin plate at z_2 might be reflected back into the substrate from another thin plate at z_1 closer to the surface. Such multiple scattering effects are not important for $Q_z \gg Q_c$ as the reflectivity for a plate gets very small in this limit, but for Q_z approaching Q_c the validity of Eq. (3.6) might be questioned. In order to elucidate this problem we show in Fig. 3.2 the

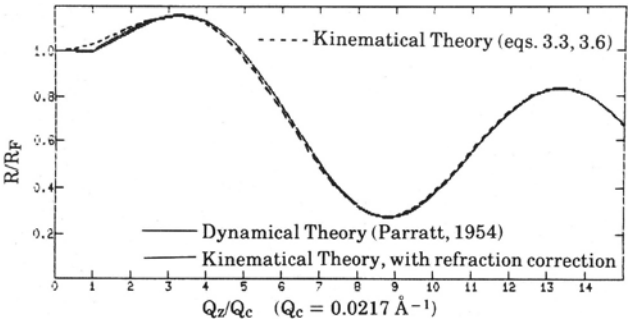

Fig. 3.2. Normalized reflectivity R/R_F versus normalized wave vector transfer Q_z/Q_c, as calculated:
---- (i) using the kinematical **master formula**, *Eq. (3.4);*
——(ii) using Eq. (3.4) with **refraction correction** *(replacing Q_z by Q_z'; and*
——(iii) using the **dynamical** *theory by Parratt[7].*
Methods (ii) and (iii) give almost identical results, while (i) differs noticeably for $Q_z < 10 \cdot Q_c$, and significantly for $Q_z < 2 \cdot Q_c$.

reflectivity of a particular density model corresponding to a typical amphiphilic monolayer on water as calculated using Eqs. (3.4) and (3.6), the so-called kinematic approximation. We now compare this to an exact calculation method devised by Parratt[7] in 1954. The model used in both calculations consists of two stratified layers of different densities. The top layer corresponds to the tail density of the film, the next layer to the head density, cf. Fig. 1.1a. At each of the three interfaces (air-tail, tail-head, head-water) both incoming and outgoing rays can be reflected or transmitted and one imposes the usual boundary conditions for the electric field of the electromagnetic wave at each interface. This results in a set of coupled linear equations which can be solved[7] for the overall reflectivity. We conclude from Fig. 3.2 that the simple kinematic approximation, Eq. (3,4), is adequate for interpreting reflectivity data from amphiphilic monolayers on water for grazing angles exceeding twice the critical angle and that the remaining discrepancy can be repaired by inclusion of the refraction correction (Q_z' instead of Q_z in Eq. (3.4)).

Before closing this section let us go back and discuss in more detail the quantity $\phi(Q_z)$, the Fourier transform of the density gradient, in the case of a

monolayer on a substrate. It is convenient to separate the density into two parts

$$\rho(z) = \rho_1(z) + \rho_2(z) \tag{3.7}$$

where $\rho_1(z) = \rho_\infty \cdot H(z)$ derives from the subphase or substrate, H(z) being the step function, and $\rho_2(z)$ is the density due to the molecules in the monolayer. The effect of interfacial diffusiness will be discussed below in sections 5 and 6. Denoting the electron density in the molecule by $\rho_m(x,y,z)$ and the average molecular area by A, $\rho_2(z)$ becomes

$$\rho_2(z) = A^{-1} \int \rho_m(x,y,z)\, dxdy \tag{3.8}$$

It follows from Eqs. (3.3), (3.4) and (3.8) that

$$\begin{aligned} \phi(Q_z) &= 1 + \rho_\infty^{-1}(iQ_z) \int \rho_2(z) \exp[iQ_z z] dz \\ &= 1 + iQ_z(\rho_\infty A)^{-1} \int \rho_m(x,y,z) \exp[iQ_z z] dxdydz. \end{aligned} \tag{3.9}$$

In terms of the molecular form factor

$$F(\mathbf{Q}) \equiv \int \rho_m(\mathbf{r}) \exp[i\mathbf{Q} \cdot \mathbf{r}] d^3r \ , \tag{3.10}$$

Eq. (3.9) becomes

$$\phi(Q_z) = 1 + iQ_z(\rho_\infty A)^{-1} F(0,0,Q_z) \ . \tag{3.11}$$

Using this form of $\phi(Q_z)$ in the master formula Eq. (3.6) for the reflectivity it is particularly transparent that the specular reflection along $\mathbf{Q} = (0,0,Q_z)$ is formed by the *interference* of waves scattered from the substrate, the first term in (3.11), and from the molecular film, the term with the molecular form factor $F(0,0,Q_z)$.

In particular, we note in passing that the substrate scattering (measured perhaps with an uncovered surface) should **not** be subtracted from experimental data as a background. The correct experimental background is found by off-setting the detector laterally from the specularly reflected beam.

4. GRAZING INCIDENCE DIFFRACTION AND BRAGG RODS

In this section we discuss the similarities and differences between information obtained by specular reflection (XR) and by grazing incidence diffraction (GID). Experimental examples are discussed in section 7 below.

For simplicity, we assume a 2D-periodic structure ("2D-crystallinity") in the monolayer film floating on the subphase: The molecules are arranged in identical unit cells which form a regular lattice. Then, in GID, Bragg diffraction occurs when the lateral scattering vector $\mathbf{Q}_{hor}$, c.f. Fig. 1.1b, coincides with a reciprocal lattice vector G_{hk}: The scattering is concentrated in so-called **Bragg Rods** (parallel to the Q_z-axis), defined by **two** Laue conditions or, in vector notation, by the equation $\mathbf{Q}_{hor} \equiv G_{hk}$. By constrast, XR

is characterised by the condition $\mathbf{Q}_{hor} \equiv 0$. The substrate gives no Bragg diffraction for $\mathbf{Q}_{hor} \neq 0$ so in GID there is no interference between the scattering from the substrate and that from the film. The substrate scattering just contributes to a flat background which can be subtracted from the total intensity to obtain the GID signal. The purpose of using grazing incidence is to minimize the background level by illuminating a depth of only a few nanometers, c.f. section 2. The GID signal, $I_{hk}(Q_z)$, is proportional to the square of the unit cell structure factor (identical to the molecular form factor, Eq. (3.10), for the case of one molecule per unit cell):

$$\text{GID:} \qquad I_{hk}(Q_z) \propto A_c^{-2} |F(G_{hk}, Q_z)|^2 , \tag{4.1}$$

where A_c is the unit cell area. Compare Eq. (4.1) for GID with the XR result:

$$\text{XR:} \qquad I_{00}(Q_z) = R_F(Q_z) \left| 1 + iQ_z (\rho_\infty A)^{-1} F(0,0,Q_z) \right|^2 . \tag{4.2}$$

Thus, XR and GID measure different parts of the monolayer structure factor, corresponding to different projections of the monolayer structure. XR corresponds to the projection of the monolayer density onto the z–axis and includes also scattering from the sub–phase. GID – with $Q_z \simeq 0$, i.e. , grazing exit as well as grazing incidence – measures the structure of the "2D–crystalline" part of the monolayer, as projected onto the x–y plane. Finally, measurement of the GID signal $I_{hk}(Q_z)$ **versus** Q_z (so–called Bragg Rod scans) gives three–dimensional information about the 2D–crystalline part of the monolayer.

We end this section with a couple of examples which further illustrate the similarities and differences between the XR and GID methods.

(i) Assume, for example that only the aliphatic tails order laterally whereas the polar heads are **laterally** "disordered". This means that the Debye–Waller factor (implicit in Eq. (3.10)) will be large and anisotropic for the "head" part of the molecule, so as to effectively make the heads invisible for $\simeq$horizontal wavevector transfers $\mathbf{Q}$. Thus, effectively, for GID the formfactor to be used is that describing the tails, - the polar heads will just contribute to the background together with the substrate. In XR the **lateral** disorder of the polar heads is irrelevant; they do indeed contribute to the average density modulation across the surface.

(ii) Another example where XR and GID give complementary rather than identical information is that of a heterogeneous film: Islands of 2D–solid phase coexisting with a non-diffracting 2D–liquid phase. The GID measures the form factor of the molecules in the solid islands whereas XR yields some sort of average density profile across the surface. The wording "some sort of average" is deliberately vague, because one must distinguish between averaging the formfactor **before** squaring in Eq. (4.2) (coherent averaging) or averaging the reflected **intensities** which is obviously required if the size of the islands is much larger than the X-ray coherence length given by $1/k_x$ and $1/k_y$ of Fig. 5.2 in the following section.

5. THERMAL ROUGHNESS OF LIQUID–VAPOUR INTERFACE

Consider in Fig. 5.1 a liquid surface confined within the area $L \times L$. A capillary wave with amplitude u_q and wavelength λ or wave vector q has been excited. The excitation energy has two origins: the surface has been enlarged, which requires the surface tension energy E_c, and liquid has been lifted from troughs to crests, which requires the gravitational energy E_g. In the bottom

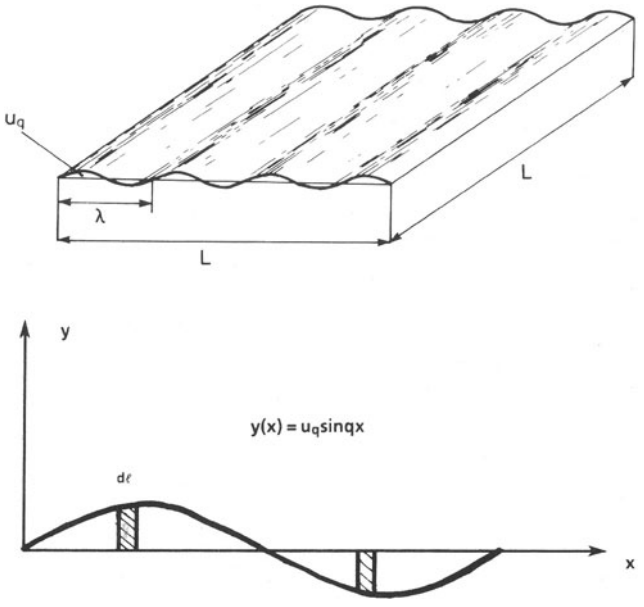

Fig. 5.1. Top: *A capillary wave, confined within the area $L \times L$, of wavelength λ or wavevector q and amplitude u_q.*
Bottom: *Side view of one wavelength. The arc-element has a length $d\ell = [1 + (dy/dx)^2]^{1/2} dx$ or approximately $[1 + \frac{1}{2}(u_q q \cos(qx))^2] dx$.*

part of Fig. 5.1 we consider one period of the wave. Note in passing that there will be L/λ such periods along the x-axis. The excess surface is $L(u_q q/2)^2 \lambda (L/\lambda)$ and the associated energy $E_c = L^2 \gamma (u_q q/2)^2$ where γ is the surface tension. The gravitational energy for one period is the integral of dE_g over half a period as the liquid in the trough in the second half of the period is lifted into the crest in the first half of the period. The entire gravitational energy is $E_g = L^2 \rho g (u_q/2)^2$. Since ρg has dimension of energy/area times an inverse length squared, it can be written as

$$\rho g \equiv \gamma k_g^2 \tag{5.1}$$

where k_g is a wave vector and therefore

$$E_q = (E_c + E_g) = \tfrac{1}{2} L^2 (u_q^2/2) \gamma (q^2 + k_g^2) . \tag{5.2}$$

Equipartition of gives the thermal average value $\langle E_q \rangle = k_B T/2$ or

$$\tfrac{1}{2} \langle u_q^2 \rangle = k_B T L^{-2} [\gamma (q^2 + k_g^2)]^{-1} . \tag{5.3}$$

Summing over all q-modes gives $\langle u^2 \rangle$:

$$\langle u^2 \rangle = \tfrac{1}{2} \sum_q \langle u_q^2 \rangle = k_B T (L/2\pi)^2 L^{-2} \int_0^{k_{max}} [(\gamma (q^2 + k_g^2)]^{-1} 2\pi q \, dq \tag{5.4}$$

or

$$<u^2> = k_B T(2\pi)^{-2}(\pi/\gamma)\log_e\left(\frac{k_{max}^2+k_g^2}{k_g^2}\right) \simeq \frac{k_B T}{2\pi}\frac{1}{\gamma}\log_e\frac{k_{max}}{k_g} . \tag{5.5}$$

In the integral over q-space we have introduced an arbitrary cut-off wavevector k_{max} which is of order π/(molecular radius).

In this derivation we have assumed that the effective surface tension is independent of wavevector. In reality this is not the case. In deriving the excess surface area of mode q we used that the line element $d\ell$ along the curved interface y(x) is $(1 + (dy/dx)^2)^{1/2}$ and we expanded the square root to first order as $(1 + (dy/dx)^2/2)$. Within this approximation the total energy is then a sum of independent, harmonic q-modes. However, with the square root expanded to higher orders one realizes that the modes are **not** harmonic: the energy of a q-mode contains all even powers of q. As long as $(dy/dx)^2 = (u_q q)^2 << 1$ the harmonic approximation is accurate for describing the excitation of one single q-mode out of the ground state, but when it comes to excite this mode out of a general, thermally excited state, the population of the other q-modes matters for calculating E_q. It is convenient to write E_q as proportional to $\gamma(q)q^2$ with an effective surface tension $\gamma(q)$ depending on q. By symmetry there cannot be any term linear in q, and the coefficient to q^2 must be proportional to k_BT, as it reflects the thermal population of the other q-modes. To order q^2 the effective surface tension $\gamma(q)$ is therefore of the form:

$$\gamma(q) = \gamma + a k_B T q^2 , \tag{5.6}$$

a being a dimensionless constant. Meunier[8] finds $a = 3/(8\pi)$. Rewriting Eq. (5.6) as

$$\gamma(q) = \gamma(1 + (q/k_m)^2) , \tag{5.7}$$

$$k_m^{-2} = a\, k_B T/\gamma \ , \ a = 3/(8\pi) , \tag{5.8}$$

we find, in analogy with Eq. (5.4)

$$<u^2> = k_B T/(4\pi^2\gamma)\int_0^\infty [(1 + (q/k_m)^2)(q^2 + k_g^2)]^{-1} 2\pi q\, dq$$

$$\simeq k_B T/(4\pi^2\gamma)\int_0^\infty [q^2 + k_g^2 + k_m^{-2}q^4]^{-1}\, 2\pi q\, dq \simeq k_B T/(2\pi\gamma)\log_e\frac{k_m}{k_g} , \tag{5.9}$$

i.e. the same form as Eq. (5.5) but with the arbitrary cut-off wavevector k_{max} replaced by the mode-mode coupling parameter k_m known from Eq. (5.8). For water the numerical values are 1.63 $Å^{-1}$ and 1.23 $Å^{-1}$, respectively. The relative difference between $\log_e(k_{max}/k_g)$ and $\log_e(k_m/k_g)$ is thus only 1.6 per cent. We now generalize this result to the case where the base surface is covered by a monolayer[8]. This layer has a certain stiffness against undulations so a fluctuation as given in Fig. 5.1 will require an additional energy of the form $\frac{1}{2}\cdot K\cdot u_q^2 q^4 \cdot L^2$. Expressing K in units of k_BT by the dimensionless number κ

$$K \equiv \kappa \cdot k_B T \tag{5.10}$$

we see immediately from (5.9) that k_m^{-2} in the integral must be replaced by

$$k_M^{-2} \equiv k_m^{-2} + K/\gamma = (a+\kappa)k_B T/\gamma . \tag{5.11}$$

The lower limit of zero in the two-dimensional integral (5.9) is an idealization which cannot be fulfilled in an actual experiment. Here one must distinguish between intensity which is specularly reflected and intensity scattered out of specular reflection by the surface roughness. This, then is a matter of the lateral wavevector **resolution** widths k_y along the direction of the beam projected onto the surface and k_x perpendicular to this direction. In practice both k_x and k_y are much larger than k_g, so the second term in the integrand in Eq. 5.9 can be neglected. The observed roughness σ is then given by

$$\sigma^2 = k_B T/(4\pi^2\gamma) \int_{k_x}^{\infty} \int_{k_y}^{\infty} [q^2 + k_M^{-2} q^4]^{-1} dq_x dq_y . \tag{5.12}$$

The integration area is indicated in Fig. 5.2 as the shaded area. In a synchrotron X-ray reflectivity experiment the resolution may well be entirely determined by the detector apertures (width w_d, height h_d) relative to the distance D between sample and detector since the incident beam collimation usually is very narrow. In that case the resolution function is box-like with dimensions as indicated in Fig. 5.2. Utilizing that the resolution perpendicular to the beam is much broader than along the beam, cf. Fig. 5.2, the integral 5.12 can again be carried out analytically[1]. The result is a roughness parameter σ which depends logarithmically on the wavevector transfer Q_z because the resolution rectangle varies linearly with Q_z:

$$\sigma^2 \simeq k_B T/(2\pi\gamma) \log_e(k_M/k_y), \qquad k_y = Q_z(h_d/D). \tag{5.13}$$

Note that neither the gravity term k_g nor the width of the detector aperture w_d appears in this final result.

Daillant et al. find in their study of a behenic acid film on water[9], that for surface pressures below 17 mN/m the action of the behenic acid film on the thermal roughness is just to diminish the surface tension from the pure water value of 72 mN/m to (72-17)mN/m = 55 mN/m and indeed they find a rms. roughness σ_{exp} varying as $\gamma^{-1/2}$ as shown in the left part of Fig. 5.3 which is reproduced from Ref. 9. Furthermore, σ_{exp} agrees with σ as calculated above without any adjustable parameters. In their original study of thermal fluctuations on a water surface Braslau et al. found[1] σ_{exp} 10% larger than σ from (5.13). Recent measurements using in situ monitoring of surface tension and ultra pure water[10] indicates that our original results[1] might have been influenced by an impure surface, both for water and carbon-tetra-chloride, and it seems as though the capillary wave model indeed accounts for the entire roughness of the surface of simple liquids like water, methanol and carbon-tetra-chloride.

Most interestingly, Daillant et al.[9] find a discontinuous decrease in $\sqrt{\gamma}\cdot\sigma$ around a surface tension of 53 mN/m. They ascribe this observation to a first order phase transition of the monolayer from a soft layer with a small value of the bending constant to a more rigid layer with a bending constant of around 200 kT. Because the observed effect only varies as the square root of the logarithm of k_M/k_y, cf. Eq. 5.13, it requires either a very rigid layer ($\kappa \gg 1$) or a low surface tension γ to significantly reduce the pure capillary wave roughness.

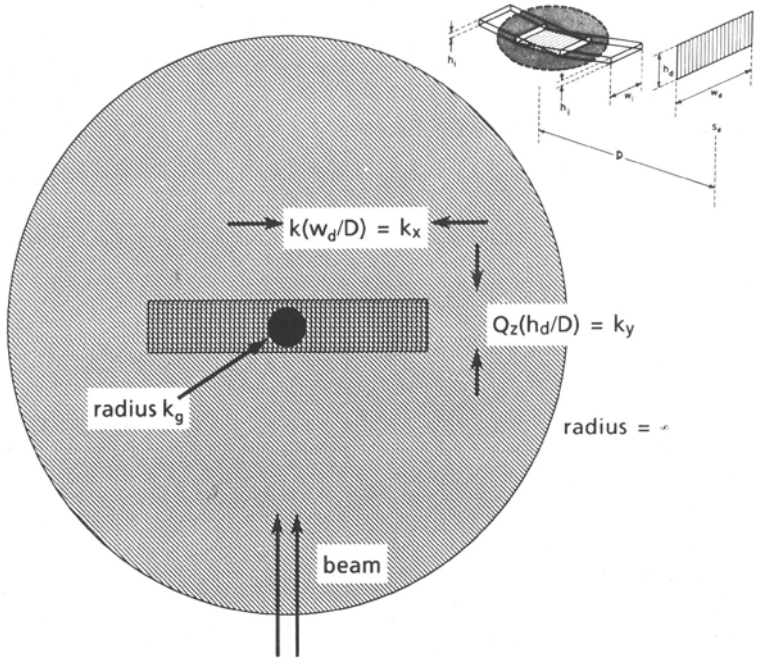

Fig. 5.2. The capillary r.m.s. roughness σ is obtained by integrating Eq. (5.12) over the whole plane except for the inner rectangle determined by the experimental resolution.

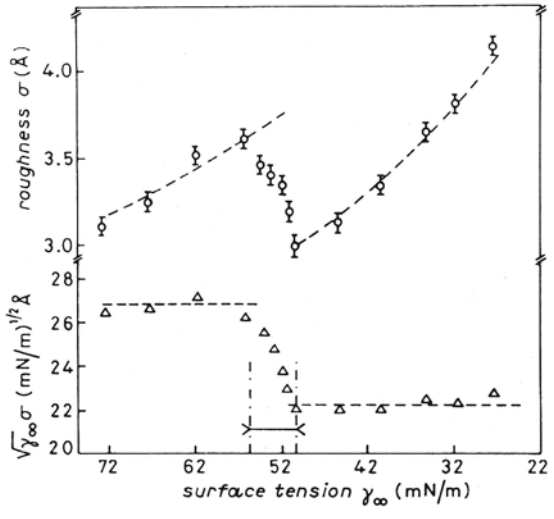

Fig. 5.3. Roughness parameter σ for a behenic acid monolayer, ref. 9. The jump at $\gamma \sim 53$ mN/m corresponds to the monolayer attaining a large rigidity against bending for $\gamma < 53$ mN/m.

6. REFLECTIVITY OF ARACHIDIC ACID FILM

The simplest monolayers may be those composed of fatty acids. The molecules consist of a hydrocarbon chain and a carboxylic acid headgroup. The lateral pressure as a function of molecular area A for one representative of this class, arachidic acid on a pure water subphase is given in the inset of Fig. 6.1. On compressing the monolayer to a molecular area of $A_t = 24$ Å^2, the lateral pressure remains below the detection limit of 1 mN/m. On further increasing the molecular density the pressure increases almost linearly with decreasing A. At a distinct pressure $\pi_s = 25$ mN/m and molecular area $A_s = 19.8$ Å^2 the pressure/area isotherm becomes very steep. The phases above and below π_s have previously been called solid and condensed liquid[4], respectively. We will show to what extent X-ray scattering provides a better picture.

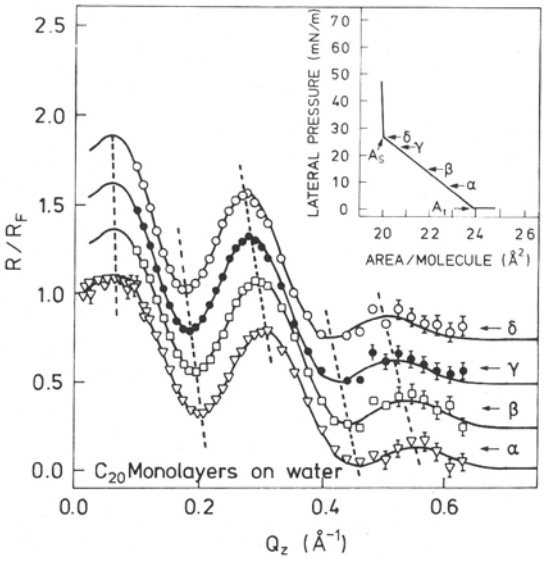

Fig. 6.1. Normalised X-ray reflectivity R/R_F vs. vertical wave vector transfor Q_z, for arachidic acid monolayers on pure water (pH 5.5, $T = 20°C$). The measurements are displaced vertically by 0.25 units and correspond to the surface pressures indicated on the isotherm of the insert.

Fig. 6.1 gives the reflectivity vs. wave vector transfers Q_z perpendicular to the surface for various surface pressures indicated as by arrows in the

isotherm. One clearly observes a shift of the extrema to lower Q_z with increasing surface pressure.

The full lines through the data points represent a simple box model of the monolayer density $\rho(z)$ with some adjustable parameters. In the model, the aliphatic tail region has a constant density ρ_T and a certain thickness l_T whereas the polar head region has density ρ_H and thickness l_H, see figure 6.2. The sharp box edges are smeared by one common Gaussian function so the

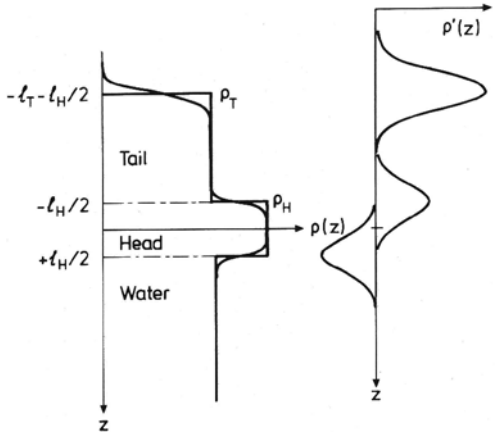

Fig. 6.2. Two-box density profile model of a Langmuir film. The boxes, describing the tail part and the polar head part respectively, are smeared by a Gaussian, as indicated by the full line. The density gradient in this model is two positive Gaussians followed by one negative Gaussian.

model contains five parameters: Two thicknesses, two densities and a smearing parameter. This model has the virtue that the Fourier transform of the density gradient can readily be written down. Let the origin be in the middle of the head group region which extends from $-\ell_H/2$ to $+\ell_H/2$ with a density of ρ_H. The tail region extends from $-\ell_T-\ell_H/2$ to $-\ell_H/2$ with a density of ρ_T. The density **gradient** is thus a set of Gaussians, all with the same width parameter σ, and located at the edges of the boxes at $z = -\ell_T-\ell_H/2$, $-\ell_H/2$ and $+\ell_H/2$. The height of each Gaussian is the **difference** between consecutive box densities. The Fourier transform of a Gaussian is a Gaussian itself, so altogether we find for the Fourier-transform, $\phi(Q) \equiv (1/\rho_\infty)\int\rho'(z)\exp(iQz)dz$, of the density gradient $\rho'(z)$ to be:

$$\phi(Q) = (1/\rho_\infty)\cdot \exp(-Q^2\sigma^2/2)$$
$$\{\rho_T\exp[-iQ(\ell_T+\ell_H/2)]+(\rho_H-\rho_T)\exp[-iQ\ell_H/2]-(\rho_H-1)\exp[iQ\ell_H/2)\}. \quad (6.1)$$

In order to obtain a direct qualitative understanding of the features in the normalized reflectivity, $R(Q)/R_F(Q) = |\phi(Q)|^2$, we shall make one further approximation in taking the tail density to be almost that of water, i.e. $\rho_T \simeq \rho_\infty$. In that case we get $\phi(Q) \simeq \phi_1(Q)$ with

$$\phi_1(Q)\exp(Q^2\sigma^2/2) = \exp[-iQ(\ell_T+\ell_H/2)\} - 2i(\rho_H/\rho_\infty-1)\sin[Q\ell_H/2]. \tag{6.2}$$

In the complex plane it is easy to visualize the two terms on the right hand side of Eq. (6.2) versus Q. The first term starts out at (1,0) for Q = 0 and then moves clockwise around the unit circle as Q increases . The second term is bound to the imaginary axis. It starts out at (0,0), then increases almost linearly with Q along the negative axis and then continues along the imaginary axis as a sine wave versus Q. Suppose for the sake of argument that $\ell_H = \ell_T$ and $\rho_H/\rho_\infty = 1.5$. For $Q(\ell_T + \ell_H/2) = \pi/2$ there is maximal constructive interference with the first term being at (-i,0) and the second term being at $(-i/2,0)$. At a 3 times larger Q there is complete destructive interference as the first term is at $(+i,0)$ and the second term is at (-i,0). At a 5 times larger Q we have again constructive interference, the first term being again at (-i,0) and the second term being at (-i/2,0) etc. When, in reality, ℓ_H is considerably smaller than ℓ_T this second constructive interference will obviously be larger than the first, as observed in Fig. 6.1. If the minimum in the reflectivity data is very pronounced, the data become very sensitive to the values of parameters, because a deep minimum simply reflects a very delicate balance in the destructive interference phenomenon. From the second term in Eq. (6.2) one also deduces that the height and depth of the reflectivity extrema depend sensitively on $(\rho_H - \rho_\infty)$. The head group density is therefore determined very accurately.

Best fit results are shown in Table 1.

Table 1. Fitted parameters of the model densities ρ(z) of Fig. 6.2, corresponding to the reflectivity data of Fig. 6.1. The densities are normalized to the density of water, $\rho_\infty = \rho_W = 0.334$ e/Å^3.

	π	A	N_T	ℓ_T	ρ_T/ρ_W	ℓ_H	ρ_H/ρ_W	N_H	σ
label	mN/m	Å^2	-	Å	-	Å	-	-	Å
δ	25.0	19.8	157	≡24.2	0.983	3.07	1.59	32	3.38
γ	21.6	20.5	≡157	23.4	0.979	3.48	1.48	35	3.22
β	15.9	21.7	≡157	22.2	0.977	3.88	1.38	39	2.99
α	11.0	22.7	≡157	32.2	0.977	4.43	1.31	44	2.93

What are reasonable dimensions of the boxes of constant density? First, consider the hydrocarbon tail. According to Ref. 11 the average distance between two CH_2 groups, projected onto the molecular axis is 1.265 Å. Each CH_2 group contains 8 electrons and is in Fig. 6.3 represented by a Gaussian distribution of width σ = 1 Å (which is certainly smaller than the final fitted smearing parameter). The neighboring CH_2 group contributes a similar Gaussian but displaced 1.265 Å along the z-axis. The last hydrocarbon group of the aliphatic tail is a CH_3 group with 9 electrons. If this is also represented by a Gaussian of the same width the height must be 9/8 of the height of the CH_2 Gaussians. As is apparent from Fig. 6.3, the molecular density is well approximated by the two-box model, provided only that the terminal CH_3 group is represented by a segment (9/8)·1.265 Å long, to give the correct

number of electrons in the tail. The tail length in the all-trans configuration is thus

$$\ell_T^0 = [n+(9/8)] \cdot 1.265\ \text{Å} \tag{6.3}$$

The z-positions of the atoms of the COOH head group are more difficult to assign. A plausible choice was made in Fig. 6.3.

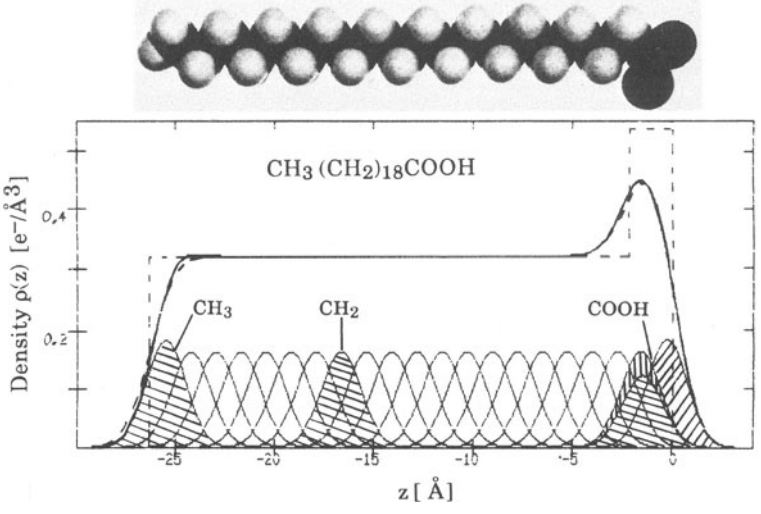

Fig. 6.3. Top: Space-filling model of the molecule.
Bottom: Full lines: Each CH_2 group is represented by a Gaussian succesively displaced by 1.265 Å. For the terminal CH_3 group and the polar head group COOH, see text.
Dashed lines: Box model and smeared box model of the density. The width parameter σ = 1 Å was chosen for display purposes. In reality, the fitted $\sigma \simeq 3$ Å.

For arachidic acid the number n of CH_2 segments is 18 and one obtains ℓ^0_T = 24.2 Å. Thus the number of fitting parameters was reduced to four. With the density ρ_T determined from the parameter fit one then calculates the number N_T of electrons in the hydrocarbon moiety according to

$$N_T = \rho_T A \ell_T \tag{6.4}$$

For the particular case one obtains $N_T = 157e^-$/molecule which has to be compared with the number $N_T = 153e^-$/molecule derived from the molecular formula $(CH_3-(CH_2)_{18})$ of the tail. This discrepancy may be an artefact introduced by the simplicity of the two box model or indicates that part of the

hydrocarbon moiety may be penetrated by water (the discrepancy corresponds to 40% of one water molecule). Now keeping the number N_T constant, independent of molecular area, ρ_T and ℓ_T are related according to Eq. (6.4) and the model parameters of table 1 are deduced using four independent fitting parameters.

The tail region thickness, ℓ_T, decreases monotonically as the area per molecule increases. This, together with the constancy of ρ_T, strongly indicates that the aliphatic tails are predominantly in the all-trans configuration and uniformly tilted. From geometric considerations one can then derive the tilt angle t by comparing the length ℓ_T of the tilted tail with the value $\ell^0{}_T$ for vertical orientation:

$$\cos t = \frac{\ell_T}{\ell_T^0} \tag{6.5}$$

One derives that on going from A_t to A_S the tilt angle t continuously decreases from about 30^0 to 0^0.

Considering the parameters in table 1 for the head group, the correlation with molecular models is more ambiguous since the hydrophilic region not only contains the carbonyl group but probably also some water. In analogy with Eq. (6.4) N_H is determined by the product of ℓ_H and ρ_H. The number of electrons in the carbonyl group COO^- is 23, so the data indicate a hydration of one water molecule per carbonyl group at the highest pressure increasing to two water molecules per carbonyl group at the lowest pressure. The decrease of ℓ_H with increasing pressure may indicate a gradual confining of the head group moieties in a plane parallel to the surface. If this ordering were perfect, ℓ_H would correspond to the dimension of a COO^- group in the direction of its symmetry axis. From molecular models one estimates values between 2.5 and 3.0 Å, not far from the value of ℓ_H at the highest pressures.

7. IN-PLANE DIFFRACTION AND BRAGG ROD DATA FROM ARACHIDIC ACID FILM

In this section we discuss grazing incidence diffraction (GID) from a monolayer of arachidic acid on water.

The geometry for GID experiments is shown in Fig. 7.1. The top view shows the footprint of the grazing incidence beam on a water/film surface as well as the specular reflected beam. The grazing incidence angle is typically 0.8 times the critical angle for total reflection so according to Eqs. (2.12), (2.8) and Fig. 2.2 the penetration depth of the evanescent wave (EW) is around $\Lambda = 1.7/Q_c$ or 77 Å. The EW is diffracted by the monolayer, and we select for detection a horizontal scattering angle of 2θ by the Soller collimator and a vertical scattering angle of α_f by the Position Sensitive Detector PSD. The signal is diffrated from the "crossed-beam-area" ABCD of the monolayer and it is clear that the signal rate is proportional to the widths of the two crossed beams. A broad Soller collimator is thus much more efficient than a slit geometry.

Let us first consider the compressed state where the molecular area is A_S and where according to the specular reflectivity data the molecules are upright. The ordered structure forms a hexagonal lattice with a corresponding reciprocal lattice as indicated by the broken lines in Fig. 7.2 (top part). The Bragg scattering selection rule (the horizontal component, $\mathbf{Q}_{hor}$, of the scattering vector must coincide with a reciprocal lattice vector $\mathbf{G}_{hk}$) implies that the scattering seen in a side view (bottom part) is confined to vertical Bragg rods through $\mathbf{G}_{hk}$. Due to the finite length L of the molecule the intensity along a Bragg rod is not constant but peaks at $Q_z = 0$ with a width of

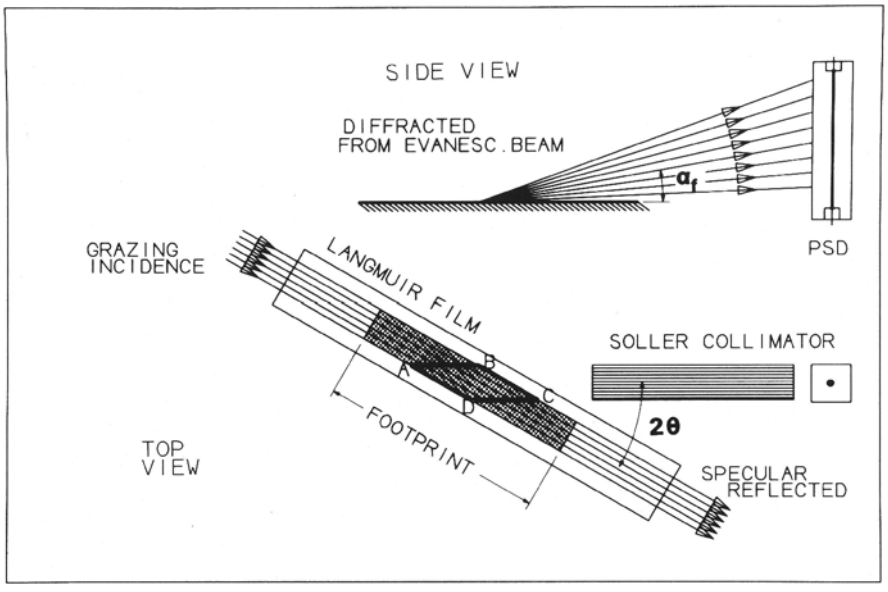

Fig. 7.1 Top view and side view of the GID geometry. The footprint of the grazing incidence beam is indicated by the darker area of the Langmuir film. The position sensitive detector PSD has its axis along the vertical direction. Only the crossed-beam-area ABCD contributes to the scattering.

order π/L. If, more specifically, we model the molecule by a cylinder of length L and diameter a, the molecular form factor along the molecular axis Q_z' is

$$S(u) = \sin(u)/u \tag{7.1}$$

with $u = Q_z' L/2$.

The radial molecular formfactor, $R(|\mathbf{Q}_r|)$, at radial $\mathbf{Q}_r$ reflects the electron distribution of the CH_2 groups projected onto a plane perpendicular to the molecular axis. Each CH_2 group has an electron distribution similar to that of oxygen and therefore its Fourier transform is approximately the atomic scattering factor of oxygen. The CH_2 groups are connected in a zig-zag line with a ~110° opening angle and a distance of 1.54 Å. The molecule is assumed to rotate freely, so the center of each CH_2 group is evenly distributed on a circle of radius $R = (1.54/2)\cos(110/2) = 0.44$ Å. The final electron distribution is the **convolution** of each CH_2 distribution with the center distribution so the Fourier transform is the **product** of the center distribution, $J_0(Q_r R)$, and the oxygen scattering factor $f_O(Q_r)$. Within the range of interest, $1.5\ \text{Å}^{-1} < Q_r < 2.0\ \text{Å}^{-1}$, the radial formfactor is well approximated by a Lorentzian in terms of the dimensionless variable $v \equiv Q_r a$

$$R(v) \propto (1+v^2)^{-1} \tag{7.2}$$

with a = 0.38 Å.

We now consider the model proposed on the basis of the reflectivity data:

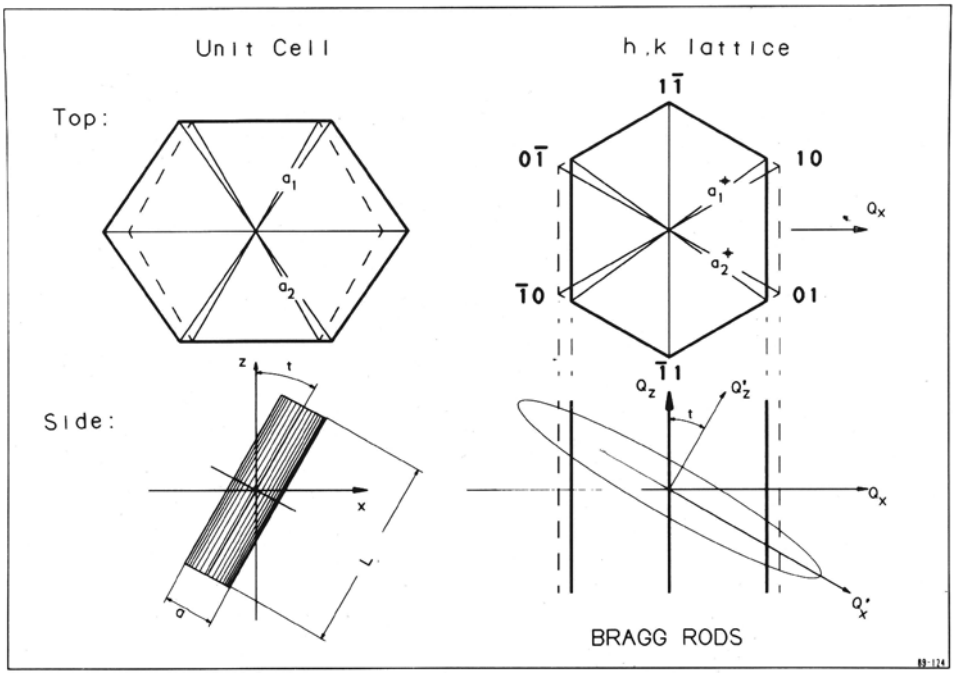

Fig 7.2 At high pressures the molecular electron density is modelled by an upright cylinder of length L and diameter a, the molecules forming a hexagonal lattice (broken line). At lower pressures the molecules tilt and the unit cell becomes distorted to a centered orthorhombic cell (full line). The lower, right panel indicates the Bragg selection rule (rods) and the formfactor of a tilted molecule (ellipse).

For pressures lower than π_s the area per molecule , A, becomes larger than A_s and the molecules tilt but **remain closed packed**, i.e., the tilt angle t is given by

$$\cos(t) = A_s/A, \tag{7.3}$$

Tilt angles t deduced from Eq. (7.3) were previously shown[12] to agree well with the values deduced from Eq. (6.5). With tilted molecules, the Bragg selection rule still holds but the molecular formfactor, indicated by the ellipse in the right bottom part of Fig. 7.2, tilts. In Fig. 7.2 a particular tilt direction (towards nearest neighbour) was chosen but in general we define the Q_x-axis as the tilt direction. In the particular case of tilting towards nearest neighbour we see from Fig. 7.2 that along the $(1,-1)$ and $(-1,1)$ Bragg rods the intensity still peaks at $Q_z=0$, whereas along the $(0,-1)$ and $(-1,0)$ rods the intensity peaks at $Q_z>0$ and that along the (1,0) to (0,1) rod at $Q_z<0$ – the latter not being observable as only scattering away from the water surface can be detected. In the cylinder model the molecular formfactor is still as given in Eq. 7.1 and 7.2 in the **molecular** frame (Q_x', Q_y, Q_z') so in the laboratory frame we insert u and v from

$$v = a \cdot |Q_y^2 + (Q_x \cos t + Q_z \sin t)^2|^{1/2} \tag{7.4}$$

$$u = (Q_z \cos t - Q_x \sin t)L/2 \tag{7.5}$$

with

$$Q_x = |G_{hk}| \cos \psi_{hk}, \qquad Q_y = |G_{hk}| \sin \psi_{hk}, \tag{7.6}$$

G_{hk} being the reciprocal lattice point considered and ψ_{hk} the angle from G_{hk} to the tilt direction. Since the sample is a two-dimensional powder the observed Bragg rod intensity, $I^{obs}(Q_z)$, contains contributions from several (h,k) reflections. The tilting of closed-packed molecules implies a distortion or strain of the hexoganal lattice to a centered orthorhombic lattice as is also indicated in Fig. 7.2, so that the optimal 2θ position for observing different (h,k) rods may split beyond the experimental resolution for sufficiently large tilt – in the example of Fig. 7.2 into a high angle peak for the $\{1,-1\}$ rod and a low angle peak for the $\{0,1\}$ and $\{1,0\}$ rods. After discussing this tutorial model let us look at the actual data in Fig. 7.3, left column. At the two highest pressures (panels c and d) there is no observable splitting in 2θ but at the two lowest pressures (panels a and b) the optimum 2θ position for the Bragg rod centered around $Q_z = 0$ (open circles) is larger than for the Bragg rod which peaks at $Q_z \approx 0.5$ Å^{-1} (crosses).

The data exhibit a very sharp peak at $Q_z \gtrsim 0$. The width is of order Q_c – the critical scattering vector for total reflection. This is an interference effect analogous to that discussed in section 2: Recall that for $2\theta = 0$ and $\alpha_i = \alpha_f \simeq \alpha_c$, the incident and total reflected beams interfere **constructively** to produce maximum intensity above and below the interface (cf. Fig. 2.2, third panel). In the present case 2θ is around 19° so clearly neither the incident nor the specular reflected beams contribute directly. Around $2\theta \simeq 19°$ the beam(s) must have undergone diffraction by the in-plane ordered structure of the monolayer. However, the diffracted rays are distributed over a range of angles α_f, c.f. Fig. 7.1, and, in particular, the diffracted rays with $\alpha_f = +\alpha_c$ and the rays diffracted into $\alpha_f = -\alpha_c$ and then total-reflected in the interface will interfere constructively. Once this mechanism is appreciated it can of course be accounted for in model calculations. In terms of $x \equiv \alpha_f/\alpha_c$ the interference effect implies a factor $V(x)$

$$V(x) = \begin{cases} 2x & \text{for } 0 < x < 1 \\ 2x/(x + (x^2-1)^{\frac{1}{2}}), & \text{for } x > 1 \end{cases} \tag{7.7}$$

in the diffracted **amplitude**, cf. Eqs. (2.6) and (2.11) and Ref. 13.

The data are compared with the tutorial model of tilted cylinders in columns 2 and 3 of Fig. 7.3. In model 1 the molecules tilt towards nearest neighbours, in model 2 towards next nearest neighbours. In both models 1 and 2 the intensity is calculated as the sum over the Bragg points (1,0),(1,0),(1,−1) etc. of $(S(u)R(v)V(x))^2$ from Eqs. 7.1-7 using tilt angles t of 7°, 14°, 20°, and 22° respectively from bottom to top. The squared structure factors are multiplied by the Gaussian smearing $\exp(-(Q_z\sigma)^2)$ with a smearing parameter of $\sigma = 1$ Å – considerably smaller than the over-all smearing of around 3 Å found in the reflectivity data as discussed further below. As cylinder length L we used the tail length of 24.2 Å from Eq. 6.3.

The tilt angles, t, were determined from Eq. 7.3, inserting for A the unit cell area A_{cell}, calculated from the observed 2θ peak positions. Apart from the smearing parameter and one over-all scale factor for all the model curves of Fig. 7.3, the only free parameter in generating the intensity profile of the Bragg rods is thus the direction of tilt. In comparing the data[14] with the model we note the following points:

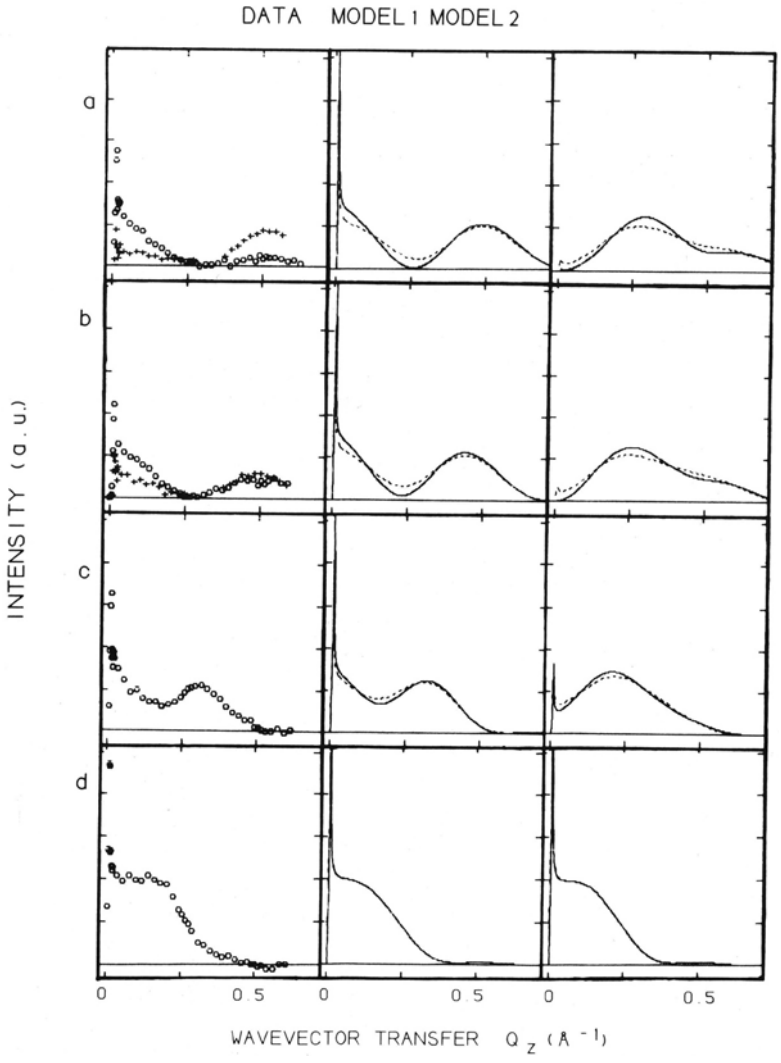

Fig. 7.3. DATA. *Arachidic acid. 2D-powder Bragg rods observed at nominal pressures of 10,16,20,21 mN/m (panels a to d, respectively). In case c and d the optimal 2θ settings for the merging peaks at $Q_z = 0$ and $Q_z > 0$ coincide, but in case a and b they split as indicated by open circles (optimum 2θ for $Q_z = 0$) and crosses (optimum 2θ for $Q_z \simeq 0.5$ Å^{-1}).*

MODELS. *Both models are the tutorial model of Fig. 7.2. In model 1 the molecules tilt towards nearest neighbours, in model 2 towards next nearest neighbours. All other parameters are essentially determined from the reflectivity data. The dashed lines represent a perturbation of the models: The molecules were tilted in a direction 8° from the symmetry directions.*

(i) Model 1 approximates the data quite well at all four tilt angles, whereas model 2 cannot at all account for the considerable intensity observed around $Q_z = 0$ for large tilt angles. The model demonstrates in a simple way that GID data are quite sensitive in determining the tilt direction as well as its magnitude.

(ii) The smearing parameter σ_{GID} is only 1 Å compared to $\sigma_{XR} = 3$ Å for the XR data. This may be related to the different coherence lengths probed in XR and GID experiments. The coherence length defines the size of the area inside which the squared deviations from ideal flatness are averaged to yield a roughness parameter σ. For XR, this has already been discussed at length in section 5. The relevant quantity for XR is the lateral Q-resolution area. In Fig. 5.2 this area is a rectangle with dimensions of the order 10^{-2} Å on one side and 10^{-3} on the other side. In GID the 2θ peak width is typically $\delta \simeq 0.3^{o} \simeq 5$ mrad, to be compared with an instrumental resolution width of 0.1^{o}. The **intrinsic** width is therefore of the order $k\delta \approx 2{\cdot}10^{-2}$ Å^{-1}, so the coherence length is much shorter in the GID experiment than in in the XR experiment. Consequently σ_{GID} may be expected to be smaller than σ_{XR}, as indeed observed experimentally.

8. CONCLUSION

The application of X-ray scattering methods to the study of the liquid-vapour interface has been developed theoretically and illustrated by experimental examples. The surfaces of simple liquids are rough due to thermally excited capillary waves. The interface can be characterized by one parameter, the rms. diffuseness, σ, which can be determined by X-ray reflectivity measurements, as illustrated for the case of water.

A liquid surface with a surfactant monolayer requires more structural parameters for its characterization. By X-ray reflectivity the densities and thicknesses of constituent sub-layers can be deduced. For rod-like arachidic acid molecules, the results could be interpreted in terms of tilted, close-packed molecules, with the tilt angle determined from a **cosine** relation, Eq. (6.5). Grazing Incidence Diffraction gives information about the lateral order in the interface: lattice spacings and correlation length. By measurement of the intensity variation along the Bragg rods, structural information complementary to that from X-ray reflectivity can be obtained. For arachidic acid monolayers, this allows determination of the tilt angle by a **sine** relation, Eq. (7.5) and figure 7.2.

Finally, we note that the methods here presented are applicable as well to **hard** interfaces, e.g., surfaces of crystalline solids or Langmuir-Blodgett films[4] of surfactant molecules on solid supports.

REFERENCES

1. A. Braslau, P.S. Pershan, G. Swislow, B.M. Ocko, J. Als-Nielsen, Phys. Rev. **A38**, 2457 (1988) and A. Braslau, M. Deutsch, P.S. Pershan, A.H. Weiss, J. Als-Nielsen and J. Bohr, Phys. Rev. Lett. **54**, 114 (1985).
2. P.S.Pershan, A.Braslau, A.H.Weiss, J.Als-Nielsen, Phys. Rev. **A35**, 4800 (1987) and references therein.
3. J. Als-Nielsen and H. Möhwald, in Handbook of Synchrotron Radiation, Vol. 4 (North Holland, eds. S. Ebashi, E. Rubinstein and M. Koch).
4. G. Gaines "Insoluble Monolayers at Liquid-Gas Interfaces", Interscience N.Y. (1966).
5. The International Tables for X-ray Crystallography, vol. 3, Kynoch Press (1962) and vol. 4 (1974).

6. B.E. Warren "X-Ray Diffraction", appendix A, Addison-Wesley (1969).
7. L.G. Parratt, Phys. Rev. **95**, 359 (1954).
8. J. Meunier, J. Phys. (Paris) **48**, 1819 (1987).
9. J. Daillant, L. Bosio, J.J. Benattar, J. Meunier, Europhys. Lett. **8**, 453 (1989).
10. P. Pershan, private communication (1989).
11. C. Tanford "The hydrophobic effect: Formation of micelles and biological membranes", Wiley, N.Y. (1973).
12. K. Kjær, J. Als-Nielsen, C.A. Helm, P. Tippmann-Krayer and H. Möhwald, J. Phys. Chem. **93**, 3200 (1989).
13. G. Vineyard, Phys. Rev. **B26**, 4146 (1982).
14. K. Kjær, J. Als-Nielsen, P. Tippmann-Krayer and H. Möhwald, to be published (1989).